(14) E. Dubois-Violette and P. G. de Gennes, *Physics (Long Island City, N.Y.)*, **3**, 181 (1967).
(15) F. Brochard and P. G. de Gennes, *Macromolecules*, **10**, 1157 (1977).
(16) E. Geissler and A. M. Hecht, *J. Phys. (Paris)*, **39**, 955 (1978).
(17) J. P. Munch, S. Candau, J. Herz, and G. Hild, *J. Phys. (Paris)*, **38**, 971 (1977).
(18) E. Geissler and A. M. Hecht, *J. Chem. Phys.*, **65**, 103 (1976).
(19) T. Tanaka, L. O. Hocker, and G. B. Benedek, *J. Chem. Phys.*, **59**, 5151 (1973).
(20) M. Nakata, T. Dobashi, N. Kuwahara, M. Kaneko, and B. Chu, *Phys. Rev. A*, **18**, 2683 (1978).
(21) F. J. Wegner, *Phys. Rev. B*, **5**, 4529 (1972).
(22) D. Patterson, *Macromolecules*, **2**, 672 (1969).
(23) K. S. Soiw, G. Delmas, and D. Patterson, *Macromolecules*, **5**, 29 (1972).
(24) T. Tanaka, S. Ishiwata, and C. Ishimoto, *Phys. Rev. Lett.*, **38**, 771 (1977).
(25) T. Tanaka, *Phys. Rev. A*, **17**, 763 (1978).
(26) H. Yamakawa, *J. Chem. Phys.*, **36**, 2295 (1962).
(27) S. Imai, *J. Chem. Phys.*, **50**, 2116 (1969).
(28) C. W. Pyun and M. Fixman, *J. Chem. Phys.*, **41**, 937 (1964).
(29) S. Imai, *Rep. Prog. Polym. Phys. Jpn.*, **8**, 9 (1965).
(30) H. Yamakawa, A. Aoki, and G. Tanaka, *J. Chem. Phys.*, **45**, 1938 (1966).
(31) M. Kurata, "Modern Industrial Chemistry", Vol. 18, Asakura Publishing Co., Japan, 1975, p 288.
(32) F. C. Chen, A. Yeh, and B. Chu, *J. Chem. Phys.*, **66**, 1290 (1977).
(33) Y. Tsunashima, K. Moro, and B. Chu, *Biopolymers*, **17**, 251 (1978).
(34) J. Ehl, C. Loucheux, C. Reiss, and H. Benoit, *Makromol. Chem.*, **75**, 35 (1964).
(35) P. Outer, C. I. Carr, and B. H. Zimm, *J. Chem. Phys.*, **18**, 830 (1950).
(36) D. E. Koppel, *J. Chem. Phys.*, **57**, 4814 (1972).
(37) Esin Gulari, Erdogan Gulari, Y. Tsunashima, and B. Chu, *J. Chem. Phys.*, **70**, 3965 (1979); B. Chu, Esin Gulari, and Erdogan Gulari, *Phys. Scr.*, **19**, 476 (1979).
(38) M. Nakata, S. Higashida, N. Kuwahara, S. Saeki, and M. Kaneko, *J. Chem. Phys.*, **64**, 1022 (1976).
(39) N. Kuwahara, M. Nakata, and M. Kaneko, *Polymer*, **14**, 415 (1973).
(40) A. Ciferri, *J. Polym. Sci., Part A-2*, 3089 (1964).
(41) Erdogan Gulari, Esin Gulari, Y. Tsunashima and B. Chu, *Polymer*, **20**, 347 (1979).
(42) B. Chu and T. Nose, *Macromolecules*, **12**, 347 (1979).
(43) G. Allen, P. Vasudevan, E. Yvonne Hawkins, and T. A. King, *J. Chem. Soc., Faraday Trans. 2*, **73**, 449 (1977).
(44) G. Rehage, O. Ernst, and J. Fuhrmann, *Discuss. Faraday Soc.*, **49**, 208 (1970).
(45) H. Yamakawa "Modern Theory of Polymer Solutions", Harper and Row, New York, 1971.

Static and Dynamical Properties of Polystyrene in *trans*-Decalin. 2. Correlation Function Profile Analysis by the Histogram Method‡

B. Chu* and T. Nose⁺

Chemistry Department, State University of New York at Stony Brook, Long Island, New York 11794. *Received March 5, 1979*

ABSTRACT: Measured single-clipped net signal photoelectron-count time correlation functions of polystyrene (NBS 705 standard, $\bar{M}_w$ = 179 300) in *trans*-decalin were analyzed by the histogram method. The line width distribution function $G(\Gamma)$ was studied as a function of concentration, temperature, and scattering angle. We observed a fast gellike mode before the overlap concentration C^* was reached. This fast gellike mode is responsible for the anomalous increase in the variance of the line width distribution in dilute solutions (as well as in the semidilute solution region) even though its magnitude can be quite small when $C < C^*$. In the semidilute region, we have identified an upper concentration range (C_g) where the hydrodynamic mode becomes vanishingly small. Finally, decomposition of the line width distribution function permits us to sketch out semiquantitatively the excess integrated intensity behavior of polystyrene in *trans*-decalin from pure solvent to pure polymer.

In a previous communication[1] and a subsequent article,[2] we have examined the static and dynamical properties of a low molecular weight polystyrene sample (NBS 705 standard, $\bar{M}_w$ = 179 300, $\bar{M}_w/\bar{M}_n$ = 1.07) in a Θ solvent, *trans*-decalin, from around the Θ temperature (20.5 °C) to 40 °C over a range of scattering angles (θ) and at different concentrations (C) from dilute solution to the semidilute and concentrated solution regions where polymer coils overlap. We shall refer to the communication[1] and the article[2] as papers 1 and 2 where pertinent references on the scaling theories as developed by de Gennes and others, the experimental methods, and results and discussion based on intensity and the cumulants method of line width analysis have been presented. By using a low molecular weight polystyrene sample in a Θ solvent, we have avoided the complication of mixing the hydrodynamic mode with internal motions of polymer segments and have concentrated our studies in ranges where Kr_g remains relatively small. $K = (4\pi/\lambda)\sin(\theta/2)$ with λ being the wavelength of light in the medium and r_g being the radius of gyration. However, at increasingly higher concentrations even before the concentration reaches the overlap concentration C^* [$=\bar{M}_w/(N_A\rho_s r_g^3)$, with $\bar{M}_w$, ρ_s, and N_A being the weight average molecular weight, the solvent density, and the Avogadro number, respectively], we have observed the variance $\mu_2/\bar{\Gamma}^2$ of the line width distribution function $G(\Gamma)$ reaching values greater than 0.5. For a polydisperse sample, the cumulants method defines the average line width $\bar{\Gamma}$ and the variance $\mu_2/\bar{\Gamma}^2$ as

$$\bar{\Gamma} = \int G(\Gamma)\Gamma \, d\Gamma \quad (1)$$

$$\mu_2 = \int (\Gamma - \bar{\Gamma})^2 G(\Gamma) \, d\Gamma \quad (2)$$

where $G(\Gamma)$ is the normalized line width distribution function and $\int G(\Gamma)\, d\Gamma = 1$. With values of $\mu_2/\bar{\Gamma}^2$ ap-

‡Work supported by the National Science Foundation.
*On leave of absence from Tokyo Institute of Technology, Tokyo, Japan.

0024-9297/79/2212-0599$01.00/0

proaching 0.5 at high concentrations and 30 °C, we are dealing with an apparent line width distribution function where the broadening in $\mu_2/\bar{\Gamma}^2$ does not come simply from individual coil size differences. Furthermore, it is no longer sufficient to use the virial equation:

$$D = D_0(1 + k_D C + ...) \quad (3)$$

to account for interactions at high concentrations. Although the cumulants method is a powerful technique for line width analysis because no a priori assumption on the form of the line width distribution function is required, we need an experimental method which permits a direct estimate of the line width distribution function. There have been many approaches used to analyze the autocorrelation function of quasielastically scattered light. The pertinent references have been listed in a review article on applications of laser light scattering to dynamics of macromolecules in solution.[3] Unfortunately, all existing methods in the literature are not applicable to our polymer line width problem. We have found the methods of Pearson and of Laplace transform unsatisfactory.[4] As the Laplace transform of a normalized signal correlation function of the scattered electric field

$$g^{(1)}(\tau) = \int_0^\infty \exp(-\Gamma\tau)G(\Gamma)\, d\Gamma \quad (4)$$

is ill-conditioned due to finite ranges (and precision) of our experiments, we have developed an approximate histogram method which does not require any assumption on the form of the line width distribution function. Furthermore, we have tested the histogram method using simulated data with unimodal ($\mu_2/\bar{\Gamma}^2$ from 0.05 to 0.15) and bimodal ($\mu_2/\bar{\Gamma}^2$ from 0.08 to 0.97) line width distributions[5] and verified it using aqueous suspensions of polystyrene latex spheres[4,5] and the same polystyrene sample (NBS 705 Standard) in cyclohexane at 35 °C.[6] In this article, we want to present our line width results of polystyrene (NBS 705 standard) in *trans*-decalin based on the newly developed histogram method of data analysis. By combining intensity and line width distribution results, we are able to identify a new gellike mode in the presence of the hydrodynamic mode. In addition, we can present in a semiquantitative way the relative magnitudes of hydrodynamic and gel-like modes over the entire polymer concentration range. Our schematic temperature–composition diagram, though only partially completed, appears to be different in certain aspects when compared with that of Daoud and Jannink.[7]

Brief Outline of the Histogram Method[4,5]

The measured single-clipped photoelectron-count autocorrelation function has the form:

$$G_k^{(2)}(\tau) = A(1 + \beta|g^{(1)}(\tau)|^2) \quad (5)$$

where k is the clipping level, τ is the delay time, A is the background, and β is assumed to be an unknown parameter in the data fitting procedure. In the histogram method,

$$|g^{(1)}(\tau)| = \sum_{j=1}^{n} a_j \int_{\Gamma_j-\Delta\Gamma/2}^{\Gamma_j+\Delta\Gamma/2} \exp(-\Gamma I\Delta\tau)\, d\Gamma \quad (6)$$

where a_j is the intensity of light contributed by the system exhibiting line widths from $\Gamma_j - \Delta\Gamma/2$ to $\Gamma_j + \Delta\Gamma/2$, n is the number of steps in the histogram, $\Delta\Gamma$ [$=(\Gamma_{max} - \Gamma_{min})/n$] is the width of each step, $\tau = I\Delta\tau$ with I and $\Delta\tau$ being the delay channel number and the delay time increment, respectively, and Γ_{max} and Γ_{min} are the stop and start of the range of the line width distribution function.

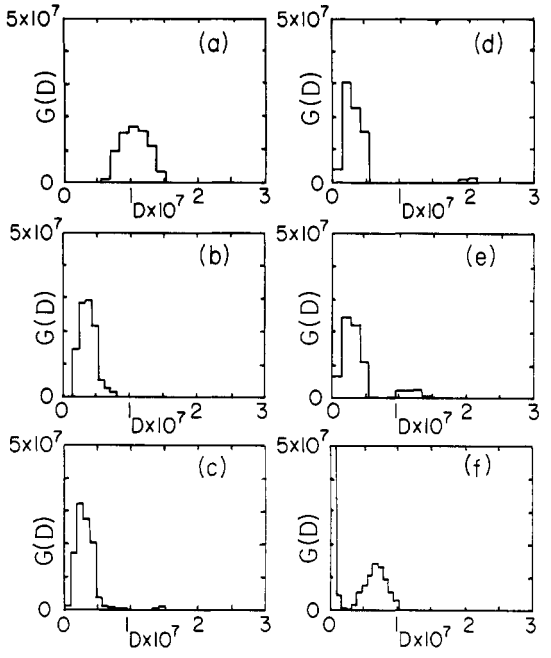

Figure 1. Plots of $G(D)$ vs. D (cm²/s) for polystyrene (NBS 705 standard) in *trans*-decalin at different concentrations, t = 20 °C, θ = 90°: (a) 0.00243 g/g of solution; (b) 0.0731 g/g of solution; (c) 0.134 g/g of solution; (d) 0.165 g/g of solution; (e) 0.233 g/g of solution; and (f) 0.346 g/g of solution.

From eq 6, we obtain a computed net signal correlation function $Y(I\Delta\tau)$ [$=A\beta|g^{(1)}(\tau)|^2$] in the form

$$Y(I\Delta\tau) = A\beta\left\{\sum_{j=1}^{n} a_j\left(-\frac{1}{I\Delta\tau}\right) \times [\exp(-(\Gamma_j + \Delta\Gamma/2)I\Delta\tau) - \exp(-(\Gamma_j - \Delta\Gamma/2)I\Delta\tau)]\right\}^2 \quad (7)$$

The values of a_j were obtained by the method of nonlinear least squares. We minimized a_j simultaneously so that $Y(I\Delta\tau)$ approximates $Y_m(I\Delta\tau)$ to within the experimental error limits.

Results and Discussion

The details of the histogram method of data analysis are presented in Figures 1, 2, and 3, where we have plotted $G(D)$ vs. D for polystyrene (NBS 705 standard) in *trans*-decalin at different concentrations, temperatures, and scattering angles, respectively. In converting the histogram from Γ space to D space, we used the simple relation $D = \Gamma/K^2$, where D is the (translational) diffusion coefficient. The numerical values from intermediate to concentrated solutions are listed in Table I. We shall first discuss the most important aspect of this study, (1) the concentration dependence, next (2) the temperature dependence, and finally (3) the angular dependence.

1. Concentration Dependence. Figure 1 shows plots of $G(D)$ vs. D at θ = 90° and 20 °C for concentrations ranging from dilute solution (C = 0.00243 g/g of solution) to the concentrated solution region (C = 0.346 g/g of solution). In the dilute solution region with concentrations changing from 0.00243 g/g of solution to 0.0731 g/g of solution, we note that Figures 1a and 1b exhibit a unimodal distribution function. However, $\bar{D}$ ($=\bar{\Gamma}/K^2$) decreases with increasing concentration indicating a negative value for k_D. Values of $\bar{D}$ computed from the cumulants method and from the histogram method agree to within 2% in dilute solution. We can compute D_0 and k_D according to eq 3 from the concentration depencence which has been discussed in 2. As the second concentration with C = 0.0731

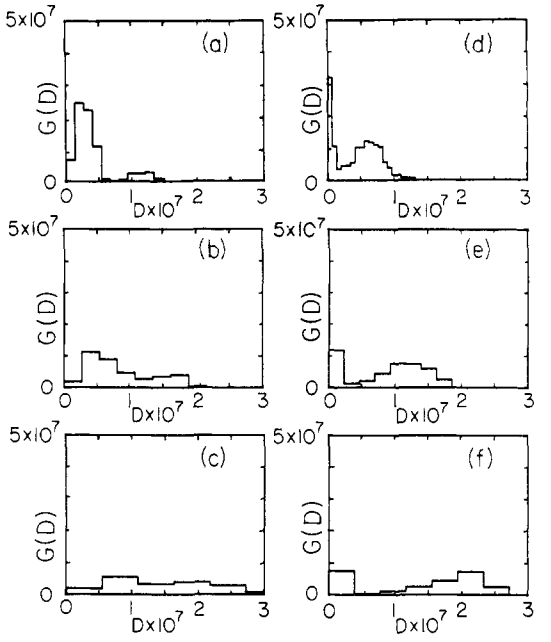

Figure 2. Plots of $G(D)$ vs. D (cm²/s) for polystyrene in *trans*-decalin at different temperatures: (a) 0.233 g/g of solution, $\theta = 90°$, $t = 20$°C; (b) 0.233 g/g of solution, $\theta = 90°$, $t = 30$ °C; (c) 0.233 g/g of solution, $\theta = 90°$, $t = 40$ °C; (d) 0.346 g/g of solution, $\theta = 135°$, $t = 20$ °C; (e) 0.346 g/g of solution, $\theta = 135°$, $t = 30$ °C; and (f) 0.346 g/g of solution, $\theta = 135°$, $t = 40$ °C.

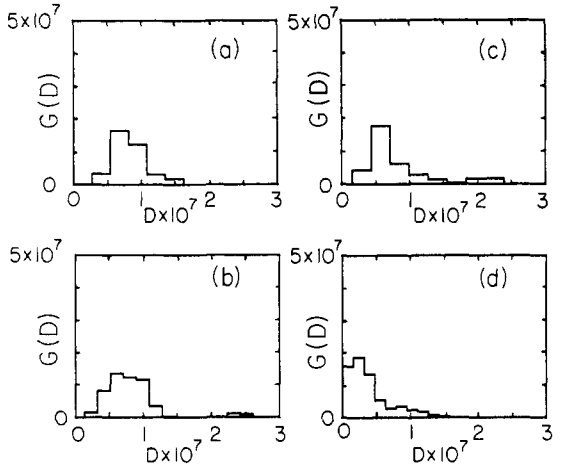

Figure 3. Plots of $G(D)$ vs. D (cm²/s) at different scattering angles: (a) 0.165 g/g of solution, $\theta = 30°$, $t = 30$ °C; (b) 0.165 g/g of solution, $\theta = 90°$, $t = 30$ °C; (c) 0.165 g/g of solution, $\theta = 135°$, $t = 30$ °C; and (d) 0.233 g/g of solution, $\theta = 135°$, $t = 20$ °C. At 20 °C, compare (1d) or (2a) with (3d) and (1f) with (2d).

g/g of solution is already fairly concentrated, we have made no attempt to compute k_D using the histogram method of data analysis.

At higher concentrations, we see the emergence of a fast gellike mode. At $C = 0.134$ and 0.165 g/g of solution, the fast mode contributes to only 1–2% of the scattered intensity. If we take

$$\int_0^\infty G(D)\,dD = \int_{\text{fast mode}} G(D)\,dD + \int_{\text{slow mode}} G(D)\,dD = \int g_f(D)\,dD + \int g_s(D)\,dD = 1 \quad (8)$$

we can write

$$A_f + A_s = 1 \quad (9)$$

where $G(D) = g_f(D) + g_s(D)$ with subscripts f and s denoting the fast and slow mode, respectively. A_f [$= \int g_f(D)\,dD$] and A_s [$= \int g_s(D)\,dD$] are the areas of the fast and the slow modes in the histograms as shown in Figures 1–3. In view of the very small contribution in A_f, we have not been able to determine $\bar{D}_f$ at $C = 0.134$ and 0.165 g/g of solution very precisely using the histogram method. However, the trends are clear. With increasing concentrations, A_f increases and $\bar{D}_f$ tends toward a lower value, as shown typically in Figure 1 from (c) to (f). Furthermore, with increasing concentrations, both A_s and $\bar{D}_s$ decrease.

In computing $\bar{\Gamma}_s$ and $\bar{\Gamma}_f$, we have also taken into account the dust problem. If we take the slow component of $G(\Gamma)$, $G_s^*(\Gamma)$, to contain a dust contribution so that

$$A_s^* = A_s' + A_d' \quad (10)$$

$$A_f^* = A_f' \quad (11)$$

Table I
Results of Histogram Analysis for NBS 705 Polystyrene in *trans*-Decalin

			$t = 20$ °C			
C, g/g of soln	0.134	0.165	0.233	0.233	0.346	0.346
θ, deg	90	90	90	135	90	135
$10^{-3}\bar{\Gamma}$, s^{-1}	2.34	2.54	3.00	4.98	3.35	5.83
$10^8\bar{D}$, cm² s^{-1}	3.18	3.44	4.01	3.90	4.39	4.48
$\mu_2/\bar{\Gamma}^2$	(0.31)	0.63	0.61	0.65		0.52
A_s	0.99	0.98	0.88	0.84	0.39	0.31
$10^{-3}\bar{\Gamma}_s$, s^{-1}	2.24	2.29	2.21	3.57	0.45	0.74
$10^8\bar{D}_s$, cm² s^{-1}	3.04	3.09	2.95	2.80	0.587	0.570
$\mu_{2s}/\bar{\Gamma}_s^2$	0.18	0.16	0.19	0.39		
A_f	0.01	0.02	0.12	0.16	0.61	0.69
$10^{-4}\bar{\Gamma}_f$, s^{-1}	1.06	1.52	0.873	1.25	0.519	0.812
$10^8\bar{D}_f$, cm² s^{-1}	14.4	20.5	11.7	9.83	6.82	6.25
$\mu_{2f}/\bar{\Gamma}_f^2$	0.0016	0.0019	0.016	0.053	0.051	0.13
			$t = 30$ °C			
C, g/g of soln	0.165	0.165	0.165	0.233	0.233	0.346
θ, deg	30	90	135	90	135	135
$10^{-3}\bar{\Gamma}$, s^{-1}	0.819	5.97	10.2	6.26	10.8	11.2
$10^8\bar{D}$, cm² s^{-1}	8.31	8.11	8.11	8.41	8.47	8.34
$\mu_2/\bar{\Gamma}^2$	0.10	0.25	0.37	0.35	0.41	0.41
A_s	1.00	0.96	0.91	0.79	[a]	0.29
$10^{-3}\bar{\Gamma}_s$, s^{-1}	0.819	5.49	8.56	4.69	[a]	1.66
$10^8\bar{D}_s$, cm² s^{-1}	8.31	7.45	6.77	6.30	[a]	1.24
$\mu_{2s}/\bar{\Gamma}_s^2$	0.10	0.11	0.17	0.24	[a]	0.44
A_f	0	0.04	0.09	0.22	[a]	0.71
$10^{-4}\bar{\Gamma}_f$, s^{-1}		1.77	2.64	1.20	[a]	1.51
$10^8\bar{D}_f$, cm² s^{-1}		24.0	21.0	16.1	[a]	11.2
$\mu_{2f}/\bar{\Gamma}_f^2$		0.0024	0.0071	0.017	[a]	0.086

	$t = 40$ °C	
C, g/g of soln	0.233	0.346
θ, deg	90	135
$10^{-4}\bar{\Gamma}$, s^{-1}	1.08	1.79
$10^8\bar{D}$, cm² s^{-1}	14.6	13.9
$\mu_2/\bar{\Gamma}^2$	(0.28)	0.39
A_s	0.58	0.30
$10^{-3}\bar{\Gamma}_s$, s^{-1}	6.84	2.61
$10^8\bar{D}_s$, cm² s^{-1}	9.25	2.03
$\mu_{2s}/\bar{\Gamma}_s^2$	0.23	0.38
A_f	0.42	0.70
$10^{-4}\bar{\Gamma}_f$, s^{-1}	1.62	2.44
$10^8\bar{D}_f$, cm² s^{-1}	22.0	19.0
$\mu_{2f}/\bar{\Gamma}_f^2$	0.041	0.058

[a] Peaks not easily separable.

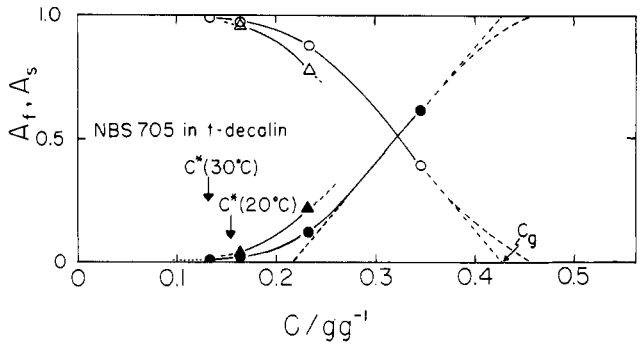

Figure 4. Concentration dependence of A_s (hollow symbols) and A_f (solid symbols). Circles denote 20 °C; triangles denote 30 °C. C_g is the (arbitrary) upper limit of the semidilute region where the hydrodynamic mode remains detectable.

where the superscript asterisk denotes the apparent values of the area determined by the histogram method in the presence of dust with $A_s^* + A_f^* = 1$. As $\bar{\Gamma}_d \ll \bar{\Gamma}_s$, we have for the apparent slow component $\bar{\Gamma}_s^*$:

$$\bar{\Gamma}_s^* = \frac{A_d'}{A_d' + A_s'}\bar{\Gamma}_d + \frac{A_s'}{A_d' + A_s'}\bar{\Gamma}_s \simeq \frac{A_s'\bar{\Gamma}_s}{A_d' + A_s'} \quad (12)$$

with $\bar{\Gamma}_f^* = \bar{\Gamma}_f$. If we take $r^* = A_f^*/A_s^*$ and $f^* = A_d'/(A_s' + A_f' + A_d') = I_d/I_t$, then we have

$$\bar{\Gamma}_s^* = (1 - f^*(1 + r^*))\bar{\Gamma}_s \quad (13)$$

where f^* can be estimated from the dust contribution in the angular distribution of scattered intensity with I_d and I_t being the scattered intensity due to dust and the total scattered intensity, respectively. For example, at 20 °C and $\theta = 90°$, $I_d/I_t = 0.075$ for $C = 0.346$ g/g of solution. The A_s and A_f values listed in Table I have been corrected for dust with A_s' and A_f' renormalized to yield eq 9.

The concentration dependence of A_s (hollow symbols) and A_f (solid symbols) at 20 °C (circles) and 30 °C (triangles) is shown in Figure 4. In addition, we have marked the location of the overlap concentration C^* at 20 and 30 °C. A very interesting aspect of this figure is the presence of a detectable fast mode even at concentrations below C^*. Thus, the gellike mode has a residual long-range effect which is present even before we reach the semidilute region. At 20 °C, there appears a linear region from C = 0.25 to 0.35 g/g of solution. At concentrations higher than 0.35 g/g of solution, we have schematically dotted in the postulated behavior and have introduced a gel concentration C_g which represents an upper limit of the semidilute region where the hydrodynamic (slow) mode remains detectable. At 30 °C, the polymer coils are more expanded. C^* occurs at a lower concentration, and we expect to have the gellike overlap behavior at a correspondingly lower concentration.

In the semidilute region ($C^* < C < C_g$), there is a range of concentration where we can expect to have the relation, such as

$$A_f \propto (C - C_0)^\delta \quad (14)$$

to hold, where C_0 and δ are the limiting concentration, if it exists, indicating the presence of A_f and an exponent, respectively. In Figure 4, we note that $C_0 < 0.12$ g/g of solution. If we use a range of C_0 varying from 0 to 0.11 g/g of solution, we observe the best range for eq 14 covering the largest range of concentration when $C_0 \to 0$, as shown in Figure 5. With $C_0 = 0$, we get $\delta = 4$.

The scattered intensity at a fixed scattering angle, e.g., $\theta = 90°$, has contributions from the slow and the fast

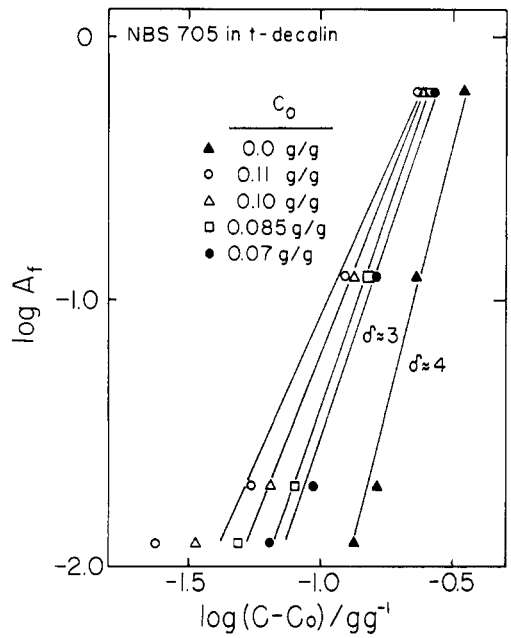

Figure 5. Log–log plots of A_f vs. $(C - C_0)$ at 25 °C and $\theta = 90°$; $A_f \propto (C - C_0)^\delta$.

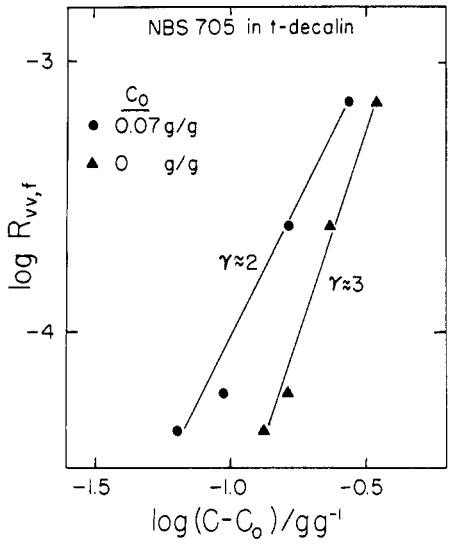

Figure 6. Log–log plots of I_f vs. $(C - C_0)$ at 25 °C and $\theta = 90°$; $\gamma = \delta + 1 - m$. If we take $m = 2$ in the concentrated solution (gel) region and $\delta \approx 4$ from Figure 5, we get $\gamma = 4 + 1 - 2 = 3$ for $C_0 = 0$. Equation 17 continues to hold for small but finite C_0.

modes in the semidilute region. In terms of absolute scattered intensity,

$$R_{vv}(\theta = 90°) = R_{vv,f}(\theta = 90°) + R_{vv,s}(\theta = 90°) \quad (15)$$

where $R_{vv,f}(\theta = 90°) = A_f(\theta = 90°)R_{vv}(\theta = 90°)$ and $R_{vv,s}(\theta = 90°) = A_s(\theta = 90°)R_{vv}(\theta = 90°)$. At high concentrations, there is only a weak angular dependence, or $R_{vv}(\theta = 90°) \approx R_{vv}(\theta = 0)$. Then, $R_{vv,f} \approx A_f R_{vv}(\theta = 0) \propto A_f C\,(\partial C/\partial \pi)_{T,P}$ or

$$R_{vv,f} \propto (C - C_0)^\gamma \quad (16)$$

With $C_0 \approx 0$ and $(\partial \pi/\partial C)_{T,P} \propto C^m$, we then have

$$\gamma = \delta + 1 - m \quad (17)$$

If we take $m = 2$ in the concentrated solution region as shown in 2 and $\delta = 4$ from Figure 5, we get $\gamma = 4 + 1 - 2 = 3$ in agreement with $\gamma \approx 3$ for $C_0 = 0$ as shown in Figure 6. However, if we take $C_0 = 0.07$ g/g of solution

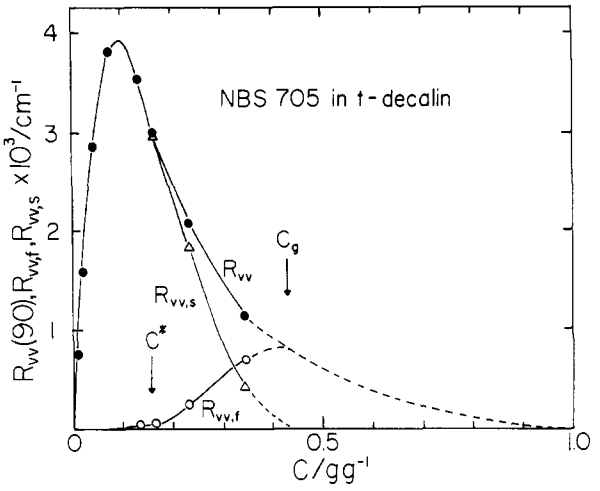

Figure 7. Plots of R_{vv} (solid circles), $R_{vv,f}$ (hollow circles), and $R_{vv,s}$ (hollow triangles) vs. concentration at $\theta = 90°$ and 20 °C. $R_{vv} = R_{vv,f} + R_{vv,s}$; $R_{vv,f} = A_f R_{vv}$; $R_{vv,s} = A_s R_{vv}$. C_g is defined in Figure 4; $C^* \equiv \bar{M}_w/(N_A \rho_s r_g^3)$. Schematically, we have neglected the density fluctuations of the polymer and of the solvent and have considered only the excess scattered intensity due to concentration fluctuations.

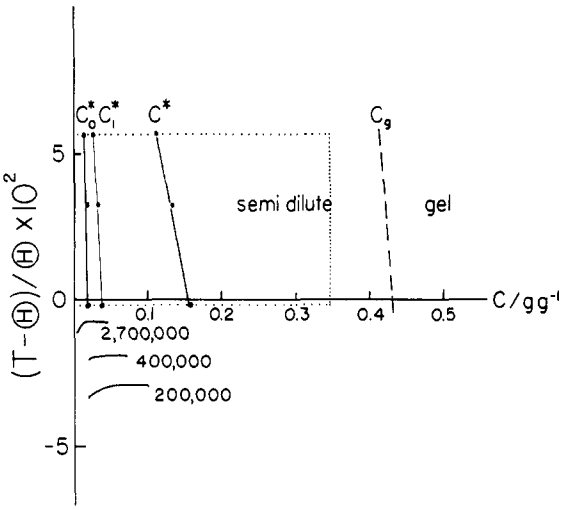

Figure 8. Temperature–concentration diagram of polystyrene in *trans*-decalin. C_g represents estimates of values extrapolated in Figure 4. The dotted rectangle represents experimental ranges of our present study. $C^* = \bar{M}_w/(N_A \rho_s r_g^3)$; $C_0^* = \bar{M}_w/[N_A \rho_s (2r_g)^3]$; and $C_1^* = \bar{M}_w/[N_A \rho_s (4/3 \pi r_g^3)]$.

and $\delta \approx 3$ from Figure 5, we again obtain $\gamma = 3 + 1 - 2 = 2$ which is consistent with the value of 2 for γ at $C_0 = 0.07$ g/g of solution. As $(\partial \pi/\partial C)_{T,P}$ does not involve a limiting C_0 value for the present polystyrene sample, we can conclude that the gellike behavior is present at low concentrations before C^* is reached. The overall scattered intensity behavior of polymer solutions can be constructed from intensity and line width measurements using the histogram method which decomposes $G(\Gamma)$ into two separate modes over a range of concentrations in the semidilute region. Figure 7 shows a plot of R_{vv} (solid circles), $R_{vv,f}$ (hollow circles), and $R_{vv,s}$ (hollow triangles) vs. concentration at $\theta = 90°$ and 20 °C. R_{vv} must increase more rapidly near $C = 0$ g/g of solution than near $C = 1$ g/g of solution because the polymer molecular weight is much greater than that of the solvent. After the total intensity has reached a maximum, the gellike mode becomes clearly measurable before the overlap concentration C^* is reached. As the contribution of the fast mode increases, the hydrodynamic mode decays with increasing concentrations. At around 0.45 g/g of solution, we have mainly the gel mode. Beyond the 0.5 g/g of solution mark, we have schematically dotted in a decaying behavior for the gel-mode intensity as the concentration reaches 100% polymer. In Figure 7, we have considered only the excess scattered intensity due to concentration fluctuations and have neglected the density fluctuations of the solvent and of the polymer. By utilizing the information from 2 and our knowledge on C^* and C_g, we have added one more line (C_g) on the temperature–composition diagram, as shown in Figure 8. This partially completed temperature–composition diagram is somewhat different from the schematic temperature–composition diagram of Daoud and Jannink.

Figure 9 shows the concentration dependence of $\bar{D}$, $\bar{D}_s$, and $\bar{D}_f$ at 20 °C and $\theta = 90°$. The overall $\bar{D}$ values do not represent the hydrodynamic diffusion coefficient in the semidilute region. In fact, $\bar{D}_s$ drops to fairly low values due to the increasing contribution of the fast mode at higher concentrations.

We shall discuss the concentration dependence of $\mu_2/\bar{\Gamma}^2$ separately in part 4.

2. Temperature Dependence. Figure 2 shows plots of $G(D)$ vs. D at different temperatures. $\bar{D}$, $\bar{D}_s$, and $\bar{D}_f$

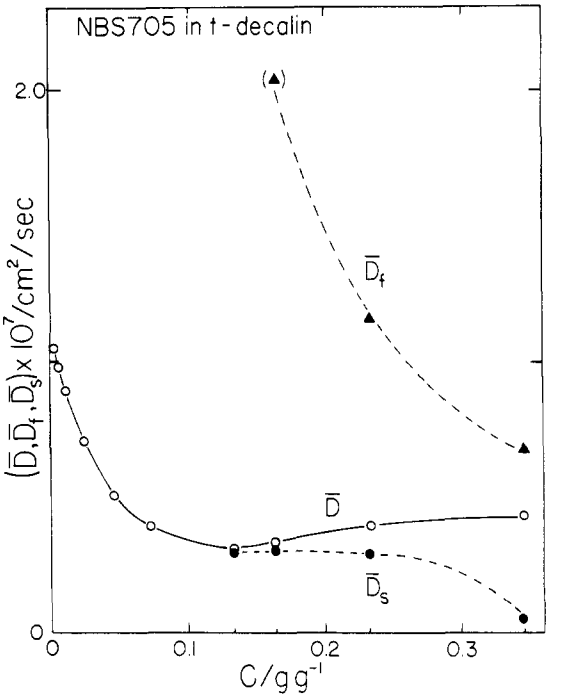

Figure 9. Concentration dependence of $\bar{D}$, $\bar{D}_s$, and $\bar{D}_f$ at 20 °C, $\theta = 90°$.

increase with increasing temperature. Figure 10 shows plots of log $\bar{D}_f$, log $(\bar{D}_f \eta_0)$, log $\bar{D}_s$, and log $(\bar{f}_s/\eta_0)$ vs. temperature at $\theta = 135°$ and $C = 0.346$ g/g of solution. We have used $\bar{f}_s/\eta_0 = (1/\bar{D}_s \eta_0)(1 - \bar{v}C^v)(\bar{M}_w/N_A)(\partial \pi/\partial C^v)_{T,P}$ where $\bar{f}_s$, η_0, $\bar{v}$, and C^v are the frictional coefficient, the solvent viscosity, the specific volume of the polymer, and the concentration in g/cm^3, respectively. At very high concentrations with $C = 0.346$ g/g of solution, $\bar{f}_s/\eta_0$ decreases slightly with increasing temperature. $\bar{D}_f$ increases with increasing temperature. This increase in $\bar{D}_f$ is implying a decrease in the correlation length with increasing temperature, rather than the temperature effect due to solvent viscosity.

3. Angular Dependence. Figure 3 shows plots of $G(D)$ vs. D at different scattering angles. For example, at $t = 30$ °C and $C = 0.165$ g/g of solution, the fast mode becomes appreciable at increasing scattering angles. Results are

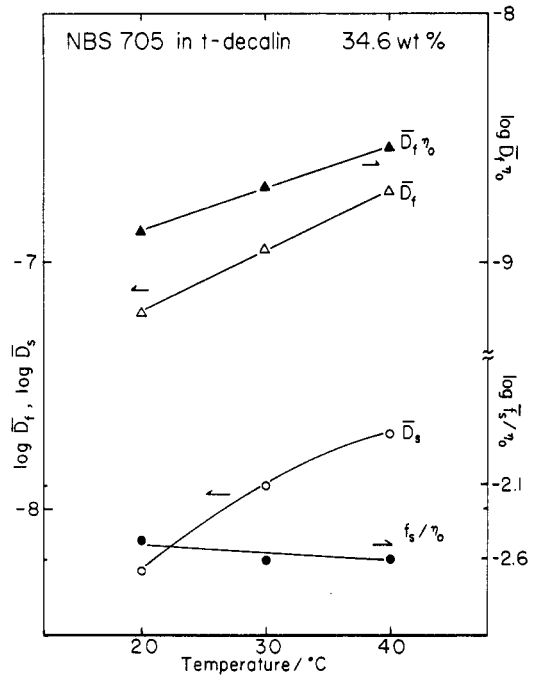

Figure 10. Plots of log $\bar{D}_f$, log $(\bar{D}_f\eta_0)$, log $\bar{D}_s$, and log $(\bar{f}_s/\eta_0)$ vs. T at 0.346 g/g of solution; $\theta = 135°$.

summarized in Figure 11a,b, where we have plotted $\bar{D}$, $\bar{D}_s$, $\bar{D}_f$, $R_{vv,s}$, and $R_{vv,f}$ as a function of sin $(\theta/2)$ at 0.165 g/g of solution and 30 °C and at 0.346 g/g of solution and 20 °C, respectively. At $C = 0.165$ g/g of solution and 30 °C, as shown in Figure 11a, $R_{vv,f}$ is barely measurable. The gellike mode contributes up to about 10% of the scattered intensity at the largest scattering angle ($\theta = 135°$) with $\lambda_0 = 488.0$ nm. $\bar{D} \approx \bar{D}_s$ over the entire angular range, and $\bar{D} = \bar{D}_s$ as $\theta \to 0$ because there $R_{vv,f}$ must be negligibly small. At $C = 0.346$ g/g of solution and 20 °C, we shall attempt to separate the intensity contribution into two components, the slow hydrodynamic mode and the fast gellike mode, as a function of scattering angle. The results are shown in Figure 11b in terms of $R_{vv,s}$ and $R_{vv,f}$ as a function of sin $(\theta/2)$. If we take $R_{vv,f} = 0$ at $\theta = 0$, we have measured $R_{vv,s}(\theta = 0) = R_{vv}(\theta = 0) = 1.17 \times 10^{-3}$ cm^{-1}. In a plot of $1/R_{vv,s}$ vs. sin^2 $(\theta/2)$, we obtain from a decomposition of angular distribution of scattered intensity an interference term $\langle r_s^2(C)\rangle$ using the equation:

$$\frac{1}{R_{vv,s}} = B\left(1 + \frac{16\pi^2}{3\lambda^2}\langle r_s^2(C)\rangle \sin^2\left(\frac{\theta}{2}\right)\right) \qquad (18)$$

$\langle r_s^2(C = 0.346$ g/g of solution$)\rangle^{1/2} = 1.2 \times 10^3$ Å. If we take $\xi_s = k_BT/6\pi\eta_0\bar{D}_s$, $\xi_s = 1.7 \times 10^3$ Å where η_0 is assumed to be the solvent viscosity and k_B is the Boltzmann constant. Two *very* qualitative observations can be made in the comparison between ξ_s and $\langle r_s^2\rangle^{1/2}$. First, ξ_s could be lower if we take the viscosity to be that of the solution. Second, if we assume the dynamical motion to be that of solid spheres, $r_s = \xi_s/1.29 = 1.3 \times 10^3$ Å, in good agreement with the value for $\langle r_s^2\rangle^{1/2}$ from a decomposition of the angular distribution of scattered intensity (eq 18). In any case, the argument is qualitative at best, as $\langle r_s^2\rangle^{1/2}$ represents a composite length for concentrated solutions, especially when the gel mode becomes appreciable. However, the agreement is nevertheless accidental. For the fast mode, we note that there is an increase in the scattered intensity $(R_{vv,f})$ with increasing scattering angles, as shown in Figure 11b. Furthermore, $\bar{D}_f$ is fairly large. If we take $\xi_f = k_BT/6\pi\eta_0\bar{D}_f$, we obtain a characteristic length of about 1.4×10^2 Å. If we take ξ_f to be the order of a characteristic spacing, we should then expect to have an increase in the scattered intensity with increasing scattering angles at small values of K, and the maximum of the scattered intensity should take place in the small-angle X-ray scattering region. This maximum could be masked partially by intensity contributions from the slow mode as we measure only the total scattered intensity. We plan to examine this interpretation further by a combination of light scattering and small-angle X-ray scattering experiments. In Figure 11b, we also note that at small scattering angles, the measured diffusion coefficient $\bar{D}$ must be identified mainly with $\bar{D}_s$ because contribution from the fast mode is small there. The $\bar{D}$, $\bar{D}_s$, and $\bar{D}_f$ behavior at a slightly lower concentration ($C = 0.233$ g/g of solution) shows similar trends as those in Figure 11b. In Figure 11c, $\bar{D}$ is closer to $\bar{D}_s$ as A_f/A_s is somewhat smaller when

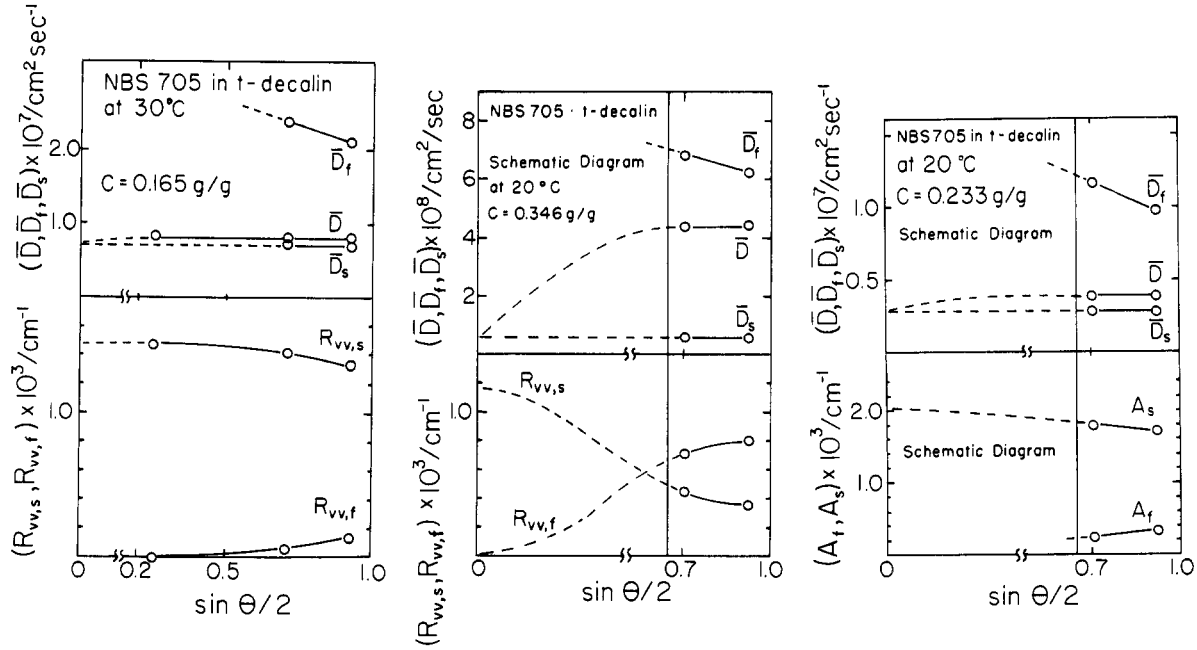

Figure 11. Plots of $\bar{D}$, $\bar{D}_s$, $\bar{D}_f$, $R_{vv,s}$, and $R_{vv,f}$ vs. sin $(\theta/2)$: (a, left) 0.165 g/g of solution, $t = 30$ °C; (b, middle) 0.346 g/g of solution, $t = 20$ °C; and (c, right) 0.233 g/g of solution, $t = 20$ °C, A_f and A_s instead of $R_{vv,s}$ and $R_{vv,f}$.

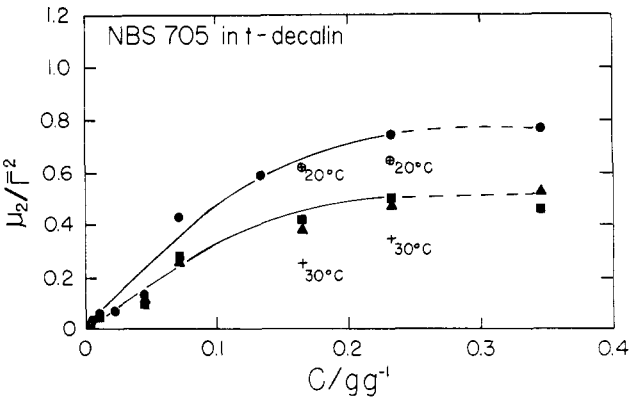

Figure 12. Plots of $\mu_2/\bar{\Gamma}^2$ vs. concentration (g/g of solution) for (NBS 705 standard) polystyrene in *trans*-decalin at 20 °C (circles), 30 °C (triangles), and 40 °C (squares); $\theta = 90°$. Solid symbols denote values from the cumulants fit; hollow symbols denote values from the histogram method; crosses denote computed values based on eq 22 at 20 and 30 °C.

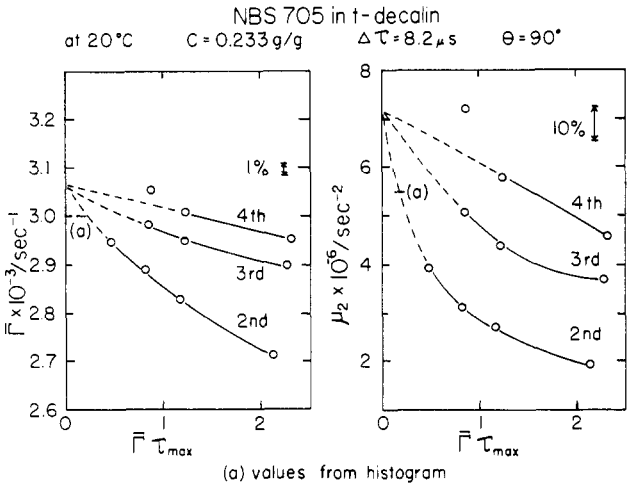

Figure 13. Plots of $\bar{\Gamma}$ and μ_2 vs. $\bar{\Gamma}\tau_{max}$ using different order of cumulants fit for polystyrene (NBS 705 standard) in *trans*-decalin at $\theta = 90°$, $t = 20$ °C, and $C = 0.233$ g/g of solution. With $\Delta\tau = 8.2$ μs, we had a total of 96 data points corresponding to $\tau_{max} = 787.2$ μs. At lower values of $\Gamma\tau_{max}$, we used fewer data points. (a) indicates the histogram result.

compared with those in Figure 11b.

In Figure 11b,c, both $\bar{D}$ and $\bar{D}_s$ appear to be independent of the scattering angle. However, $\bar{D}_f$ decreases with increasing scattering angle indicating that $\bar{\Gamma}_f$ may not have a K^2 dependence. This fact is enforced by the observation that A_f increases with increasing K making $\bar{\Gamma}_f \propto K^P$ where $P < 2$.

4. Concentration Dependence of the Variance $\mu_2/\bar{\Gamma}^2$. Figure 12 shows plots of $\mu_2/\bar{\Gamma}^2$ vs. concentration at 20 °C (circles), 30 °C (triangles), and 40 °C (squares). We note that the values from the cumulants fit (solid symbols) do not agree well with those from the histogram fit (hollow symbols) when $\mu_2/\bar{\Gamma}^2$ values are fairly high. We should consider the results of the cumulants fit to be approximate because of the extrapolation procedure used in the data analysis. Figure 13 shows plots of $\bar{\Gamma}$ and μ_2 vs. $\bar{\Gamma}\tau_{max}$. A proper way to obtain $\bar{\Gamma}$ and μ_2 is to fit the net signal correlation function using the same number of data points measured at different delay time increments by different order cumulants fits. From a plot of $\bar{\Gamma}$ or μ_2 which is fitted using different order of cumulants expansion vs. τ_{max}, we can try to obtain the correct value. In our case, as we were mainly interested in the qualitative feature of the $\mu_2/\bar{\Gamma}^2$ vs. concentration curve, we measured the correlation function at only one delay time. Then we tried to obtain $\bar{\Gamma}$ and μ_2 from extrapolations to $\bar{\Gamma}\tau_{max} = 0$. However, in the fitting procedure, as we reduced τ_{max}, we had to reduce the number of data points. The resultant extrapolation tends to yield values of $\bar{\Gamma}$ and μ_2 which represent an upper bound for the correct values. In Figure 13, we have also shown the results from the histogram method which is much more reliable in dealing with bimodal or broad line width distribution functions.

The high values of $\mu_2/\bar{\Gamma}^2$ can be interpreted in terms of the bimodal distribution.

By definition,

$$\mu_2 = \int G(\Gamma)(\Gamma - \bar{\Gamma})^2 \, d\Gamma \tag{19}$$

As $G(\Gamma) = g_s(\Gamma) + g_f(\Gamma)$, we have

$$\bar{\Gamma} = \int G(\Gamma)\Gamma \, d\Gamma = \int [g_s(\Gamma) + g_f(\Gamma)]\Gamma \, d\Gamma = A_s\bar{\Gamma}_s + A_f\bar{\Gamma}_f \tag{20}$$

where A_s $[=\int g_s(\Gamma) \, d\Gamma]$ and A_f $[=\int g_f(\Gamma) \, d\Gamma]$ are the normalization factors for $g_s(\Gamma)$ and $g_f(\Gamma)$ with $A_s + A_f = 1$. We have, in fact, used eq 20 in expressing eq 12. Then, by substituting eq 20 into the definition for μ_2, we have

$$\mu_2 = \int G(\Gamma)[(A_s + A_f)\Gamma - (A_s\bar{\Gamma}_s + A_f\bar{\Gamma}_f)]^2 \, d\Gamma = \int G(\Gamma)[A_s(\Gamma - \bar{\Gamma}_s) + A_f(\Gamma - \bar{\Gamma}_f)]^2 \, d\Gamma = \int G(\Gamma)[A_s^2(\Gamma - \bar{\Gamma})^2 + A_f^2(\Gamma - \bar{\Gamma}_f)^2 + 2A_sA_f(\Gamma - \bar{\Gamma}_s) \times (\Gamma - \bar{\Gamma}_f)] \, d\Gamma \tag{21}$$

Integration of the terms in eq 21 over the range of $G(\Gamma)$ yields

$$\mu_2 = A_fA_s(\bar{\Gamma}_f - \bar{\Gamma}_s)^2 + A_s\mu_{2s} + A_f\mu_{2f} \tag{22}$$

where μ_{2s} $[=A_s^{-1}\int g_s(\Gamma)(\Gamma - \bar{\Gamma}_s)^2 \, d\Gamma]$ and μ_{2f} $[=A_f^{-1}\int g_f(\Gamma)(\Gamma - \bar{\Gamma}_f)^2 \, d\Gamma]$ are the second moments of the slow and fast modes, respectively. We can rewrite

$$\mu_2 = \mu_2^* + \mu_2^{**} \tag{23}$$

where

$$\mu_2^* = A_fA_s(\bar{\Gamma}_f - \bar{\Gamma}_s)^2 \tag{24}$$

and

$$\mu_2^{**} = A_s\mu_{2s} + A_f\mu_{2f} \tag{25}$$

Equation 24 is the dominating term in eq 23. Thus, the main contribution for a large μ_2 comes from the square of the difference in line width $(\bar{\Gamma}_f - \bar{\Gamma}_s)^2$. We have tabulated the values of $\mu_2/\bar{\Gamma}^2$, $\mu_2^*/\bar{\Gamma}^2$, $\mu_2^{**}/\bar{\Gamma}^2$, $\mu_{2s}/\bar{\Gamma}_s^2$, and $\mu_{2f}/\bar{\Gamma}_f^2$ as a function of concentration at $\theta = 90°$ and two different temperatures (20 and 30 °C) in Table II. Values of $\mu_2/\bar{\Gamma}^2$ were computed from the line width distribution $G(\Gamma)$ determined by the histogram method. $\mu_2^*/\bar{\Gamma}^2$ and $\mu_2^{**}/\bar{\Gamma}^2$ were computed according to eq 24 and 25. Indeed, for large values of $\mu_2/\bar{\Gamma}^2$, the $\mu_2^*/\bar{\Gamma}^2$ term has provided the major contribution even though individual $\mu_{2s}/\bar{\Gamma}_s^2$ and $\mu_{2f}/\bar{\Gamma}_f^2$ values remain relatively small. The angular dependence of $\mu_2/\bar{\Gamma}^2$ can be attributed to the increasing importance of the gellike mode. For example, at $\theta = 90°$ and $C = 0.165$ g/g of solution, $\mu_2/\bar{\Gamma}^2 = 0.25$ with $\mu_2^*/\bar{\Gamma}^2 = 0.16$, while at $\theta = 135°$, $\mu_2/\bar{\Gamma}^2$ increases to 0.37, but the main contribution comes from $\mu_2^*/\bar{\Gamma}^2$ which has a value of 0.26.

Finally, in our histogram analysis, we know that we can determine $\bar{\Gamma}_s$ and $\bar{\Gamma}_f$ more accurately than A_f and A_s, especially when one of the peaks is very small.[5] In Table III, we have shown computed values of A_f based on $\bar{\Gamma}$ values estimated from the cumulants fit and $\bar{\Gamma}_s$ and $\bar{\Gamma}_f$ values from the histogram method with

$$A_{f,c} = (\bar{\Gamma} - \bar{\Gamma}_s)/(\bar{\Gamma}_f - \bar{\Gamma}_s) \tag{26}$$

Table II
Comparison of $\mu_2/\bar{\Gamma}^2$, $\mu_2^*/\bar{\Gamma}^2$, $\mu_2^{**}/\bar{\Gamma}^2$, $\mu_{2s}/\bar{\Gamma}_s^2$, $\mu_{2f}/\bar{\Gamma}_f^2$ at Different Concentrations and Scattering Angles

(a) Concentration Dependence

	C, g/g of soln			
	0.134	0.165	0.233	0.346
	$t = 20\,^\circ$C; $\theta = 90^\circ$			
$\mu_2/\bar{\Gamma}^2$	0.31	0.63	0.61	
$\mu_2^*/\bar{\Gamma}^2$	0.16	0.50	0.51	0.48
$\mu_2^{**}/\bar{\Gamma}^2$	0.15	0.13	0.10	
$\mu_{2s}/\bar{\Gamma}_s^2$	0.18	0.16	0.19	
$\mu_{2f}/\bar{\Gamma}_f^2$	0.002	0.002	0.016	0.051

	C, g/g of soln		
	0.165	0.233	0.346
	$t = 30\,^\circ$C; $\theta = 90^\circ$		
$\mu_2/\bar{\Gamma}^2$	0.25	0.35	(0.41)[a]
$\mu_2^*/\bar{\Gamma}^2$	0.16	0.23	(0.30)[a]
$\mu_2^{**}/\bar{\Gamma}^2$	0.09	0.12	(0.11)[a]
$\mu_{2s}/\bar{\Gamma}_s^2$	0.11	0.24	(0.44)[a]
$\mu_{2f}/\bar{\Gamma}_f^2$	0.002	0.017	(0.086)[a]

(b) Angular Dependence

	θ, deg		
	30	90	135
	$t = 30\,^\circ$C; $C = 0.165$ g/g of solution		
$\mu_2/\bar{\Gamma}^2$	0.10	0.25	0.37
$\mu_2^*/\bar{\Gamma}^2$	0	0.16	0.26
$\mu_2^{**}/\bar{\Gamma}^2$	0.10	0.09	0.11
$\mu_{2s}/\bar{\Gamma}_s^2$	0.10	0.11	0.17
$\mu_{2f}/\bar{\Gamma}_f^2$		0.002	0.007

[a] $\theta = 135^\circ$.

where the subscript c denotes the computed value. The agreement further illustrates the consistency of our analysis.

Conclusions

In choosing a relatively low molecular weight polystyrene sample and in dissolving it in a Θ solvent, we have, in fact, concentrated our studies using fairly contracted polymer coils which exhibit an extended semidilute solution region. By realizing the fact that the variance of the line width distribution is unusually high, we come to the development of a new approximate histogram method of correlation function profile analysis. The advantage of the histogram method is that we do not have to make any a priori assumption on the form of the line width distribution function and that the method is valid for determining an approximate bimodal distribution function in Γ space. With this new method, we can explain the large values of $\mu_2/\bar{\Gamma}^2$ as mainly due to the presence of a fast gellike mode even though its magnitude can be quite small. Here we use the word "fast" with reference to the slower hydrodynamic mode. The interesting aspect of this observation is the presence of gellike behavior at concentrations before C reaches C^* where coil overlap occurs. We have examined the concentration, temperature, and scattering angle dependence of the dynamical behavior of polystyrene (NBS 705 standard) in *trans*-decalin. Figures 7 and 8 are particularly important. In Figure 7, we have presented (and sketched in) the excess scattered intensity behavior of a polymer solution from pure solvent to pure polymer. According to our viewpoint, we have a semidilute region between C^* and C_g. Beyond C_g, only the gel mode remains. Thus, the temperature–composition diagram appears to behave differently than that initially predicted by Daoud and Jannink. The scaling theory is valid at infinite molecular weight. In our case, we can clearly see that power law relations are valid only for limited ranges of concentration. Finally, we have linked line width measurements with integrated scattered intensity studies. By a decomposition of the angular distribution of scattered intensity, we note that there are two characteristic lengths governing the two separate hydrodynamic and gellike modes. It is important to point out that many of the effects we have observed will not be seen easily by the same instrument if we take a high molecular weight polymer sample. Experiments at large Kr_g ranges are in progress.

Table III
Comparison of A_f (Histogram Method) and $A_{f,c}$ (eq 26)

			$t = 20\,^\circ$C			
C, g/g of soln	0.134	0.165	0.233	0.233	0.346	0.346
θ, deg	90	90	90	135	90	135
A_f (histogram)	0.012	0.020	0.12	0.16	0.61	0.69
$A_{f,c}$[a]	0.025	0.026	0.13		0.67	0.73

			$t = 30\,^\circ$C		
C, g/g of soln	0.165	0.165	0.165	0.233	0.346
θ, deg	30	90	135	90	135
A_f	0	0.040	0.092	0.22	0.71
$A_{f,c}$		0.053	0.11	0.23	0.73

	$t = 40\,^\circ$C	
C, g/g of soln	0.233	0.346
θ, deg	90	135
A_f	0.42	0.70
$A_{f,c}$	0.46	0.71

[a] $A_{f,c} = (\bar{\Gamma} - \bar{\Gamma}_s)/(\bar{\Gamma}_f - \bar{\Gamma}_s)$ with $\bar{\Gamma}$ from cumulants fit.

References and Notes

(1) B. Chu and T. Nose, *Macromolecules*, **12**, 347 (1979).
(2) T. Nose and B. Chu, *Macromolecules*, previous paper.
(3) B. Chu, *Phys. Scr.*, **19**, 458 (1979).
(4) B. Chu, Esin Gulari, and Erdogan Gulari, *Phys. Scr.*, **19**, 476 (1979).
(5) Esin Gulari, Erdogan Gulari, Y. Tsunashima, and B. Chu, *J. Chem. Phys.*, **70**, 3965 (1979).
(6) Erdogan Gulari, Esin Gulari, Y. Tsunashima, and B. Chu, *Polymer*, **20**, 347 (1979).
(7) M. Daoud and G. Jannink, *J. Phys. (Paris)*, **37**, 973 (1976).